ORIGINAL PAPER

Carbon quantum Dot@Silver nanocomposite–based fluorescent imaging of intracellular superoxide anion

Haixia Liang[1] · Hongwei Liu[2,3] · Baohua Tian[1,2] · Risheng Ma[1] · Yongzhen Wang[2]

Abstract

Silver nanoparticle (Ag NP)–coated carbon quantum dot (CQD) core-shell-structured nanocomposites (CQD@Ag NCs) were developed for fluorescent imaging of intracellular superoxide anion ($O_2^{\bullet-}$). The morphology of CQD@Ag NCs was investigated by transmission electron microscopy, and the composition was characterized by X-ray diffraction and X-ray photoelectron spectroscopy. CQDs display blue fluorescence with excitation/emission maxima at 360/440 nm, and the fluorescence was quenched by Ag NPs in CQD@Ag NCs. In the presence of $O_2^{\bullet-}$, Ag NPs were oxide-etched and the fluorescence of CQDs was recovered. A linearity between the relative fluorescence intensity and $O_2^{\bullet-}$ solution concentration within the range 0.6 to 1.6 μM was found, with a detection limit of 0.3 μM. Due to their high sensitivity, selectivity, and low cytotoxicity, the as-synthesized CQD@Ag NCs have been successfully applied for imaging of $O_2^{\bullet-}$ in MCF-7 cells during the whole process of autophagy induced by serum starvation. In our perception, the developed method provides a cost-effective, sensitive, and selective tool in bioimaging and monitoring of intracellular $O_2^{\bullet-}$ changes, and is promising for potential biological applications.

Keywords CQD@Ag NCs · $O_2^{\bullet-}$ · Core-shell · Nanoprobe · Fluorescence recovery

Introduction

As a primary radical and precursor of all reactive oxygen species, excessive superoxide anion ($O_2^{\bullet-}$) may cause oxidative stress leading to cell damage and death [1–3]. Various nanostructured electrodes-based electrochemical sensors, such as Co-PCC/SPCE, Ti_3C_2-ATP-$Mn_3(PO_4)_2$, ZIF-8-derived carbon, Ag NPs/MWNTs, $FePO_4$/rGO-C, and hollow porous PtAg, have been well established to determine $O_2^{\bullet-}$ [4–9]. Among these nanomaterials, silver nanoparticles (Ag NPs) exhibit outstanding non-enzymatic catalytic performance for $O_2^{\bullet-}$ reduction. Also, Ag NPs have many prominent advantages over traditional immobilization of superoxide dismutase–based methods, such as easy preparation, good sensitivity, high selectivity, and chemical and thermal stabilities [10]. Despite advantages of wide linear range, low detection limit, excellent selectivity, and good stability in detection of $O_2^{\bullet-}$ [11, 12], there are still some substantial drawbacks to the electrochemical method with Ag NPs. It has displayed the deficiencies of targeting at extracellular $O_2^{\bullet-}$ and incapability of imaging, especially as an optical imaging strategy for $O_2^{\bullet-}$ in living cells.

To solve the above problems, the fluorescence method combined with Ag NPs provides good opportunities for imaging detection of $O_2^{\bullet-}$ in living cells, owing to its good sensitivity, high spatial and temporal resolution, easy operation, and capability of real-time monitoring in living cells [13]. As for now, many fluorescent probes for $O_2^{\bullet-}$ detection have been reported, including hydroethidine (HE) [14] and dihydrorhodamine 123 [15], CDs-HE [16], FITC@$mSiO_2$@$hmSiO_2$@HE [17], Au@Ag NRs [18], and the two-photon fluorescent probe

Haixia Liang and Yongzhen Wang contributed equally to this work.

Electronic supplementary material The online version of this article (https://doi.org/10.1007/s00604-020-04359-8) contains supplementary material, which is available to authorized users.

✉ Haixia Liang
lianghaixia456@hotmail.com

✉ Yongzhen Wang
wangyongzhen@tyut.edu.cn; https://orcid.org/0000-0003-0615-1136

[1] College of Biomedical Engineering, Taiyuan University of Technology, Jinzhong 030600, China

[2] College of Material Science and Engineering, Taiyuan University of Technology, Taiyuan 030024, China

[3] College of Chemistry and Chemical Engineering, Taiyuan University of Technology, Taiyuan 030024, Shanxi, China

[19]. However, these fluorescent small molecule–based and hydroethidine-based probes usually suffer from the limitation of complex design, tedious synthetic preparation, the interference from background fluorescence, and non-specific staining with other oxidants, resulting in poor selectivity and sensitivity [20]. Meanwhile, due to their own optical properties, imaging of Au@Ag NRs and two-photon fluorescent probe needs dark-field microscopy and two-photon fluorescence microscopy [21], respectively. These microscopic imaging equipment are uncommon that hinders their practical applications in biological and medical labs.

Carbon quantum dots (CQDs) have attracted increasing attention and emerged as a novel type of fluorescent imaging nanoprobe due to their good membrane permeability, low toxicity, favorable biocompatibility, and stable fluorescence [22–25]. With assistant reductants, carbon-based dots could serve as both the reductant and stabilizer for in situ growth of Ag NPs attributed to their surface reducing and hydrophilic functional groups [26, 27], which provides simple composition of CQD and Ag NP hybrids. Carbon and metal nanocomposites both possess nature of their own, which were developed as a turn-on fluorescent probe [28–30]. In the turn-on model, the fluorescence of CQDs was quenched by the medium-sized (5 nm) Ag NPs and recovered when etched by oxidant.

In this study, core-shell CQD@Ag nanocomposites (NCs) were designed and synthesized as illustrated in Scheme 1. We adopted a one-step hydrothermal synthesis strategy to prepare CQDs with high fluorescence emission. CQD@Ag NCs were formed by in situ chemical reduction. The fluorescence of CQDs was quenched by the silver shell due to their proximity. With the production of $O_2^{\bullet-}$, the silver shell can be effectively etched by $O_2^{\bullet-}$ and thus CQDs can be released, leading to the recovery fluorescence of CQDs. After evaluation of
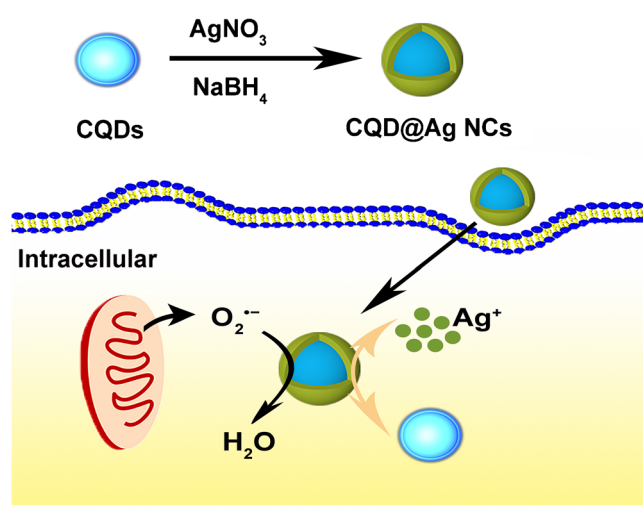
Scheme 1 Summary of one-step preparation of CQD@Ag NCs and schematic illustrations of fluorescence "turn-on" detection $O_2^{\bullet-}$ based on CQD@Ag NCs in living cells

sensitivity, selectivity, and cytotoxicity, the synthesized CQD@Ag NCs were used for fluorescence imaging of intra-cellular $O_2^{\bullet-}$.

Experiment

Chemical and materials

Citric acid (CA) and urea (UA) were obtained from Shengtai Chemical Reagent Co., Ltd. (Tianjin, China, http://tjdongli05302.11467.com). Silver nitrate (AgNO$_3$) was purchased from Sailboat Chemical Reagent Technology Co., Ltd. (Tianjin, China, http://www.tjhxsj.cn). Sodium borohydride (NaBH$_4$) was purchased from Tianjin Chemical Reagent Co., Ltd. (Tianjin, China, http://www.tjfch.com). Hypoxanthine and xanthine oxidase were purchased from Yuanye Biotechnology Co., Ltd. (Shanghai, China, http://www.shyuanye.com/index.html). Disodium hydrogen phosphate dodecahydrate (Na$_2$HPO$_4$), potassium chloride (KCl), potassium phosphate dibasic (KH$_2$PO$_4$), and sodium chloride (NaCl) were obtained from Kaitong Chemical Reagents Co., Ltd. (Tianjin, China, http://tjkthxsj.china-j.com). Phosphate-buffered saline (8 g L^{-1} NaCl, 0.2 g L^{-1} KCl, 1.44 g L^{-1} Na$_2$HPO$_4$, 0.24 g L^{-1} KH$_2$PO$_4$, pH 7.2, sterilized at 121 °C for 20 min). Roswell Park Memorial Institute 1640 was obtained from Sigma-Aldrich (Shanghai, China, https://www.sigmaaldrich.com). Fetal bovine serum (FBS) was purchased from Tianhang Biotechnology Co., Ltd. (Zhejiang, China, http://www.hzsjq.com). EBSS-Earle's salts were provided by Hosai Technology Co., Ltd. (Qingdao, China, http://www.haosail.com). MTT Cell Proliferation and Cytotoxicity Detection Kit was purchased from Solarbio Technology Co., Ltd. (Beijing, China, http://www.solarbio.com/). MCF-7 cells were obtained from Shanxi University. The ultrapure water used throughout all experiments was purified with a Millipore system which was all 18.2 MΩ cm^{-1} (URT-11-10T, Mill-Q, China). Other reagents were all of analytical grade and were commercial products. No further purification was carried out in this experiment.

Synthesis of CQDs and CQD@Ag NCs

CQDs were hydrothermally synthesized using citric acid as precursor and urea as nitrogen source [31]. The synthesis of CQDs is improved on the basis of predecessors. The specific synthetic procedure is shown in the Electronic Supporting Material.

CQD@Ag NCs were synthesized according to the method shown in Scheme 1. Briefly, 0.8 mg solid CQDs and 0.72 mg sodium borohydride (NaBH$_4$) were dissolved in 5 mL ultra-pure water. Then, 5 mL of 4 mM AgNO$_3$ solution was slowly dropped into the mixtures of CQDs and NaBH$_4$ solution

followed by magnetic agitation for 30 min. After the color of the solution changed from pale yellow to dark brown, CQD@Ag NC solution was obtained. The final products were first purified by centrifugation at 10,000 rpm for 20 min. The precipitates were dried at $-80\ °C$ for 48 h and solid sample of CQD@Ag NCs was reserved.

Instruments

Surface morphology and size of CQDs and CQD@Ag NCs were characterized by a JEM-2010 transmission electron microscopy (JEOL, Japan, https://www.jeol.co.jp/) with an accelerating voltage 200 kV. The relative height was performed on a Park NX10 atomic force microscopy (AFM, Suwon, South Korea, https://parksystems.com/cn/). X-ray diffraction (XRD) patterns about CQDs and CQD@Ag NCs were received from a Rigaku D/Max-3B X-ray diffractometer (XRD, Japan, https://www1.rigaku.com/ja). The fluorescence spectra were obtained from a FluoroMax-4 fluorescence spectrometer (Horiba, Japan, https://www.horiba.com/). The chemical compositions of CQDs and CQD@Ag NCs were analyzed by X-ray photoelectron spectroscopy (XPS, ESCALAB 250Xi Thermo Scientific, http://corporate.thermofisher.com). Fourier transform infrared (FT-IR) spectra were recorded to analyze the functional groups of CQDs and CQD@Ag NCs by using ALPHA II Fourier transform infrared spectrometer (Bruker, Germany, https://www.bruker.com/). Fluorescence microscopic images of cells were taken with a Leica fluorescence microscope (Leica, Germany, https://www.leica-microsystems.com.cn/cn/). Photographs were recorded using a digital camera under a UV lamp (365 nm excitation).

Fluorescence response of CQD@Ag NCs to various concentrations of $O_2^{•-}$ solution

According to the previous studies, the enzymatic reaction of xanthine oxidase (XO, 200 mU mL^{-1}) and hypoxanthine (HX, 100 μM) can generate a stable 2 μM L^{-1} $O_2^{•-}$ [32–34]. The various concentrations of $O_2^{•-}$ samples were prepared by changing the concentration of XO (0–200 mU mL^{-1}) into phosphate-buffered saline with constant mild stirring. CQDs (100 μg mL^{-1}) and CQD@Ag NCs (100 μg mL^{-1}) were added into the reaction solution which produced $O_2^{•-}$ and incubated at 37 °C for 10 min, respectively. The corresponding fluorescence spectra of the reaction solution were measured by a FluoroMax-4 fluorescence spectrometer with the excitation at 360 nm (emission at 440 nm). The fluorescence intensity was termed F_0, and the fluorescence intensity of CQD@Ag NCs etched by different concentrations of $O_2^{•-}$ was termed F. The correlation between the ratio of fluorescence intensity (F/F_0) and the concentration of $O_2^{•-}$ was established .

Cell culture and MTT detection

MCF-7 cells were cultured in Roswell Park Memorial Institute 1640 (RPMI-1640) containing high glucose supported by 10% fetal bovine serum (v/v), 100 μg mL^{-1} streptomycin, and 100 units mL^{-1} penicillin at 37 °C under a 5% CO_2 atmosphere. MCF-7 cells were seeded in 96-well plates with a density of 1×10^4 cells per well in medium, and incubated 12 h under 37 °C in a 5% CO_2 condition. The cytotoxicity of CQD@Ag NCs was tested as follows. First, MCF-7 cells were incubated in culture media with the addition of CQD@Ag NCs at 5,10, 20, 30, 50, 100, and 200 μg mL^{-1} for 24 h. Control groups were treated under the same conditions with the addition of CQDs. Then, cells were washed with the phosphate-buffered saline, and the fresh culture media (100 μL) containing 10 μL MTT (5 mg mL^{-1}) were dropped to each well and incubated for another 4 h. Subsequently, the supernatant was removed, followed by the additional 110 μL of DMSO in each well and shaken for 10 min. The optical density (OD) was obtained at 490 nm on a microplate reader. The cell viability was determined using the following formula: cell viability (%) = ($OD_{treated}/OD_{control}$) × 100%. For the experiments of selectivity test, the details of experiment about interference analysis are shown in the Electronic Supporting Material.

In vivo fluorescence detection and imaging

CQDs and CQD@Ag NCs were used as a nanoprobe for fluorescence imaging. The cultured MCF-7 cells were plated on a Petri dish in advance 24 h before fluorescence imaging studies in living cells. MCF-7 cells were seeded in 24-well plates at a density of 10^4 cells per well and incubated for 1 h before treatment. Next, the cells were incubated at 37 °C for 30 min in 200 μL of culture media containing 10 μL CQD@Ag NCs (100 μg mL^{-1}) solutions and 10 μL CQDs (100 μg mL^{-1}), respectively. Then, the MCF-7 cells were washed with phosphate-buffered saline (pH = 7.4) three times to remove the residual nanoprobes and continuously cultured in fresh medium for 0, 30, 60, 90, and 120 min. The fluorescence imaging was obtained by a fluorescence microscope with excitation at 365 nm wavelength. For determining the generated $O_2^{•-}$ during autophagy in living cells, EBSS-Earle's salts were added to induce the generation of $O_2^{•-}$ and fluorescence microscopic images were then acquired after being induced at different times (0, 30, 60, 90, 120 min).

The fluorescence images were analyzed and calibrated using ImageJ 1.51j8 (Bethesda, USA, https://imagej.nih.gov/ij/index.html). About 30 cells were counted for each experimental group. The area of interest (AOI) of each cell was defined as round 400 square pixels region (3 AOIs per cell). Average pixel fluorescence intensity of each cell was calculated for 3 AOIs.
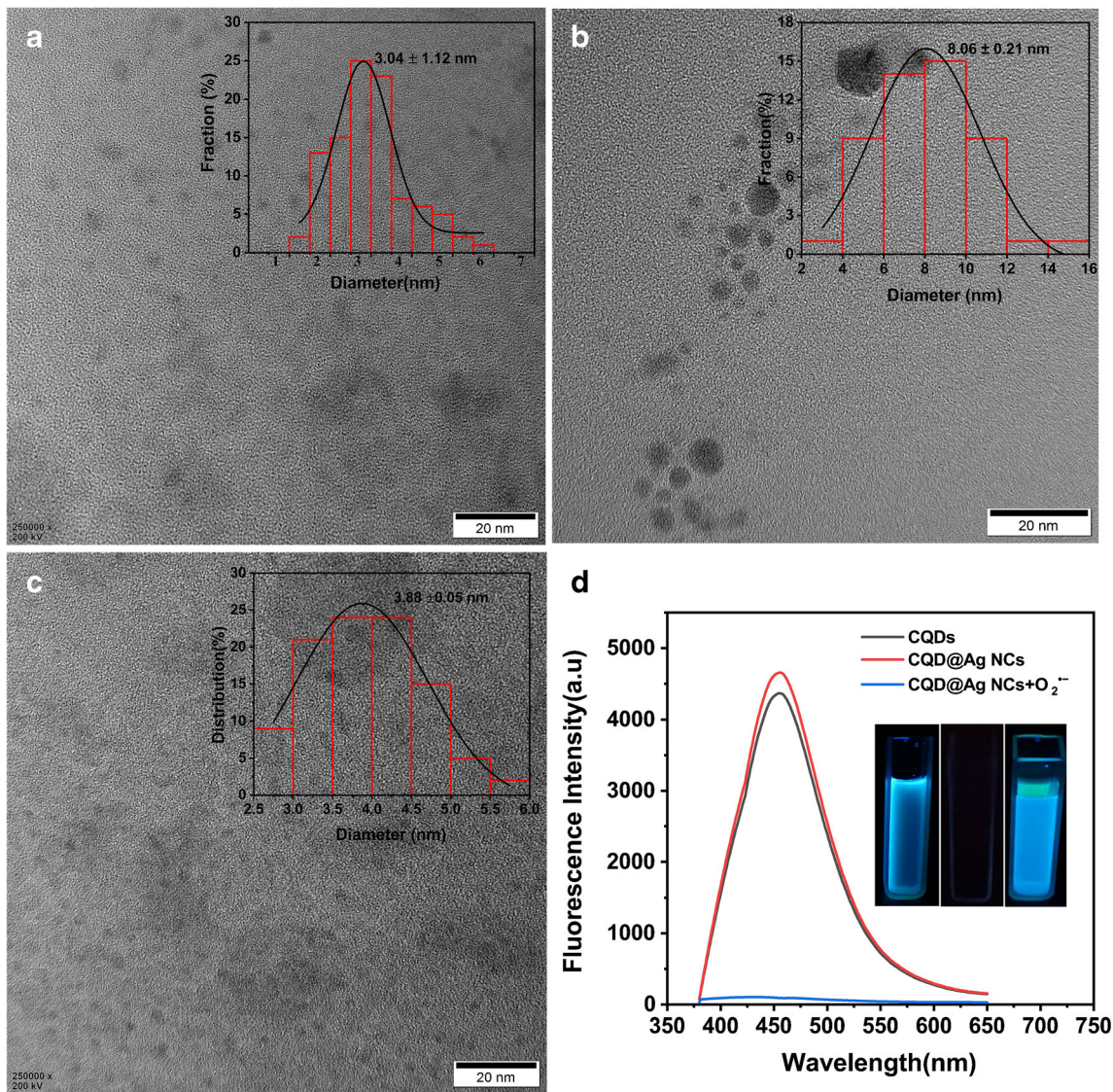
Fig. 1 TEM images of **a** CQDs, **b** CQD@Ag NCs, and **c** CQD@Ag NCs after etching by $O_2^{\cdot-}$, respectively (scale bars, 20 nm) and insets are the size distributions (**a**, **b**, and **c**, respectively). **d** Fluorescence emission spectrum of CQDs, CQD@Ag NCs, and CQD@Ag NCs etched by $O_2^{\cdot-}$; insets are the photographs of CQDs, CQD@Ag NCs, and CQD@Ag NCs etched by $O_2^{\cdot-}$ under 365 nm UV light

Fig. 2 **a** XRD patterns of CQDs and CQD@Ag NCs. **b** Ag3d XPS spectra of CQD@Ag NCs
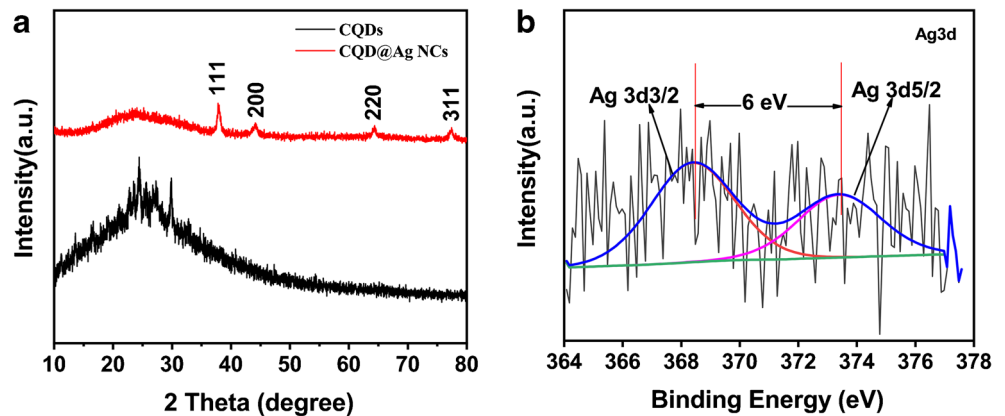
Fig. 3　a Fluorescence emission response to increasing concentrations of $O_2^{\bullet -}$. **b** Plot of F/F_0 (the ratio of CQD@Ag NC fluorescence intensity to CQDs) versus concentrations of $O_2^{\bullet -}$ (0, 0.2, 0.4, 0.6, 0.8, 1.0, 1.2, 1.4, 1.6, 1.8, 2.0, 2.4, 2.8 μM). Inset: plot of linear region from 0.6 to 1.6 μM. The error bars were estimated from three replicate measurements
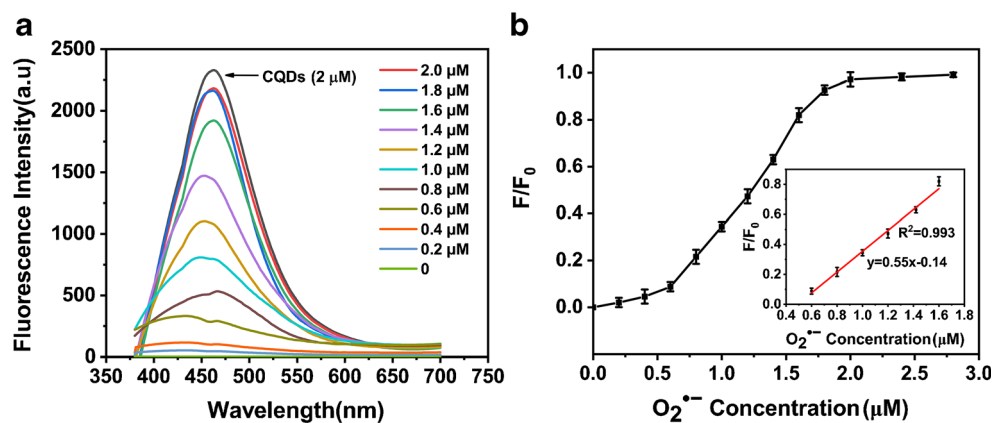
Results and discussion

Characterization of CQDs and CQD@Ag NCs

CQDs were prepared by hydrothermal synthesis, and CQD@Ag NCs were synthesized by in situ reduction of silver nanolayer on the surface of CQDs. The morphologies of CQDs and CQD@Ag NCs were characterized by TEM. As shown in Fig. 1a, the CQDs were smooth and well dispersed with the average diameter of 3.04 ± 1.12 nm, while the surface of CQD@Ag NCs (Fig. 1b) became rough and well dispersed with the average diameter of 8.06 ± 0.21 nm, which was larger after the introduction of the silver nanolayer on the surface of CQDs. The results indicated the formation of a certain thickness of silver nanolayer on the surface of the CQDs. AFM images are shown in Fig. S1 a and b, the increase in relative height of CQD@Ag NCs, compared with CQDs, which further indicate the formation of CQD@Ag NCs. The TEM image of CQD@Ag NCs after being etched by $O_2^{\bullet -}$ is shown in Fig. 1c, and it is clearly seen that the morphologies are spherical and the average size of these nanoparticles is 3.88 ± 0.05 nm and is close to CQDs, demonstrating the CQDs were released after being etched by $O_2^{\bullet -}$. To illustrate the fluorescence properties of CQDs and CQD@Ag NCs, fluorescence spectra are shown in Fig. 1d. The emission peak of CQDs located at 440 nm when excitation wavelength was 360 nm. The fluorescence of the CQDs was quenched by silver when the CQD@Ag NCs are formed that may result from the local

surface plasmon resonance in Ag NPs [35]. The fluorescence reproduced in CQD@Ag NC solution with oxidative etching by $O_2^{\bullet -}$. This is consistent with its fluorescent photograph under 365 nm UV light.

The chemistry composition and surface functional groups of CQDs and CQD@Ag NCs were investigated by XRD, XPS, and FT-IR spectra. The typical XRD patterns of CQDs and CQD@Ag NCs are depicted in Fig. 2a. CQDs exhibited a broader peak centered at $2\theta = 27°$ [36], which indicates that the structures of CQDs are amorphous carbon structures. The peaks at $2\theta = 38°$, $44°$, $65°$, and $78°$ can be assigned to (111), (200), (220), and (311) diffractions, respectively, of the face-centered cubic lattice of Ag (JCPDF 04-0783) [37], suggesting the synthesis of pure crystalline silver on the CQD surface. XPS was applied to characterize the element composition and chemical state of material's surface layers. The longitudinal split of the 3d doublet of Ag is deduced to be 6.0 eV (Fig. 2b), which confirms the formation of silver nanolayers. Composition variety in C1s spectrum of CQDs (Fig. S3a) and CQD@Ag NCs (Fig. S3b), indicating the reduction of C=O groups into C–OH on CQDs by in situ reduction of Ag NPs. Compared with CQDs in FT-IR spectra (Fig. S2), the stretching vibration of C=O (1650 cm^{-1}) decreases and C–OH (1375 cm^{-1}) increases in CQD@Ag NCs, which confirmed the reduction of C=O into C–OH groups. The variety of O1s spectrum in CQDs and CQD@Ag NCs (Fig. S3c and S3d) [38] further demonstrated the improved stability of the CQD@AgNCs by in situ composite between the Ag NPs

Table 1　An overview on recently reported nanomaterial-based optical methods for determination of superoxide anion

Materials	Method applied	Linear range (μM)	Detection limit (nM)	Intra/extracellular	Ref.
CD-HE	Ratiometric fluorescence	0.5–140	100	Intracellular	[16]
FMH NPs	Ratiometric fluorescence	0.2–20	80	Intracellular	[17]
PCLA-$O_2^{\bullet -}$	Chemiluminescence	$0–9.5 \times 10^{-4}$	0.0193	Intracellular	[41]
PS-SO$_3$H@Tb/G	Ratiometric fluorescence	1.012×10^{-2}–6.0	3.4	Extracellular	[42]
Au NDs	Fluorescence	0.6–78	445	Intracellular	[40]
CdTe QDs-Schiff base	Fluorescence	2–100	1800	Extracellular	[39]
CQD@Ag NCs	Fluorescence	0.6–1.6	300	Intracellular	This work

and the surface oxygen sites of CQDs. These XPS results reveal that the CQD@Ag NCs were successfully synthesized by in situ reduction. Some related data are described in the Electronic Supporting Material.

Sensitivity investigation for different concentrations of $O_2^{\bullet-}$ solution

For evaluation of the detection sensitivity, the fluorescence emission spectra of the solution with different concentrations of $O_2^{\bullet-}$ ranging from 0 to 2 μM were measured. As shown in Fig. 3a, the fluorescence intensity is gradually enhanced with increasing $O_2^{\bullet-}$ concentration, displaying $O_2^{\bullet-}$ dose-dependent fluorescence enhancement. In order to better simulate the fluorescence response of CQD@Ag NCs to various concentrations of $O_2^{\bullet-}$ solution, fluorescence intensity of CQD@Ag NCs (F) was normalized to that of CQDs (F_0). Normalization of fluorescence intensity of CQD@Ag NCs to that of CQDs could reduce accidental errors caused by operation errors, transmittance differences among cuvettes, and different fluorescence excitation efficiency. Figure 3b shows the calibration curves based on F/F_0 versus $O_2^{\bullet-}$ concentration, and the inset shows that there is a narrow relationship between the relative fluorescence intensity and the $O_2^{\bullet-}$ concentration in the range of 0.6–1.6 μM. The linear regression equation is $F/F_0 = 0.55c\ (O_2^{\bullet-}) - 0.14$ with a correlation coefficient $R^2 = 0.993$, deriving the detection limit of 0.3 μM. A comparison of linear range and detection limit with previous optical methods based on nanomaterials for $O_2^{\bullet-}$

detection is shown in Table 1. It can be found that the CQD@Ag NC–based detection method exhibits lower detection limit than the other two fluorescent nanomaterial–based assays [39, 40], while higher than that based on ratiometric fluorescent and chemiluminescent nanomaterials [16, 17, 41, 42]. Compared with all these methods, the CQD@Ag NCs exhibit narrow linear range and low sensitivity [16, 17, 39–42], according to the above formula for linear regression. Precisely because the range of response became narrow; the slope of the linear regression equation also became small when normalization of fluorescence intensity.

Cytotoxicity and selectivity of CQD@Ag NCs for imaging of the $O_2^{\bullet-}$ in living cells

In order to study the biocompatibility of the fluorescent probe, MTT detections were used to evaluate the cytotoxicity of CQDs and CQD@Ag NCs. The results indicated that MCF-7 cells still kept high viability after incubating for 24 h with either CQDs or CQD@Ag NCs up to 200 μg mL^{-1} (Fig. 4a). In other words, if the concentration of probes was not more than 200 μg mL^{-1}, then both CQDs and CQD@Ag NCs had low toxicity to cells and could be used for intracellular fluorescent detection and imaging as nanoprobes.

Additionally, Fig. 4b exhibits the fluorescence images of MCF-7 cells in different inducing conditions. MCF-7 cells incubated with CQDs exhibit bright blue fluorescence

Fig. 4 **a** Cell viability of MCF-7 cells incubated with CQDs and CQD@Ag NCs for 24 h. **b** The selectivity detected by fluorescence microscopy images for $O_2^{\bullet-}$ and different interferences containing H_2O_2, UA, DA, and glucose. MCF-7 cell incubation with CQD@Ag NCs (100 μg mL^{-1}) and CQDs (100 μg mL^{-1}) for 30 min and induced by different interferences
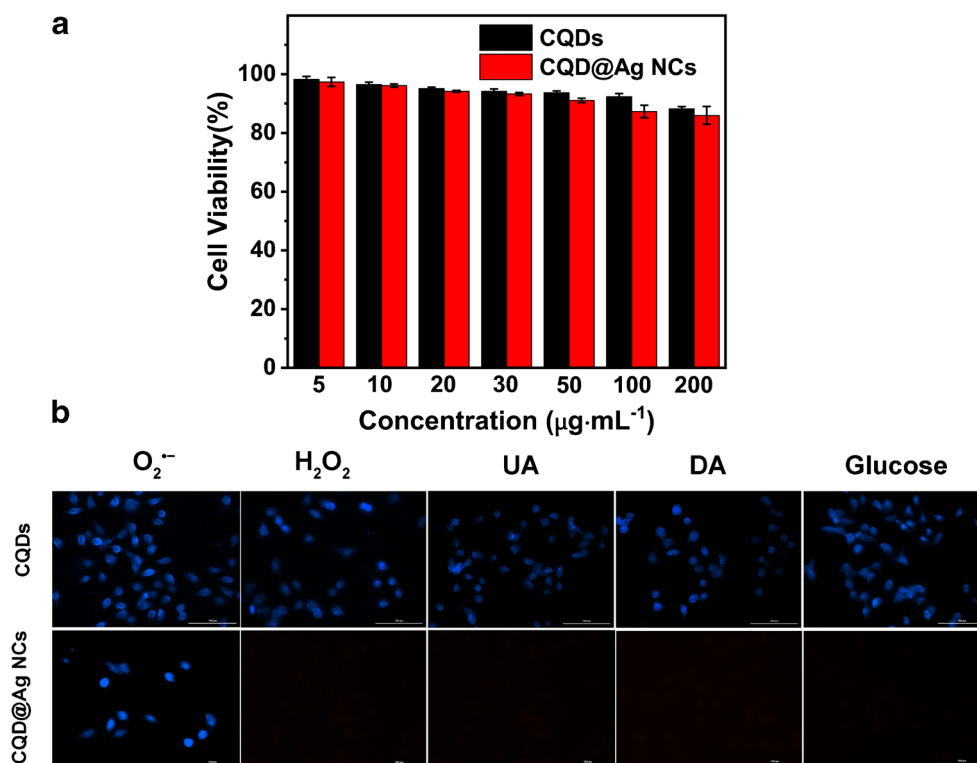
induced by $O_2^{\bullet-}$, DA, H_2O_2, and glucose, respectively. In stark contrast, no obvious fluorescence except induced by $O_2^{\bullet-}$ was observed in different conditions. This indicates there was no noticeable interference from UA, DA, glucose, and H_2O_2 in relation to the response generated by $O_2^{\bullet-}$, suggesting that the CQD@Ag NCs possess excellent selectivity for the fluorescence detection and imaging in living cells.

Fluorescent imaging of intracellular $O_2^{\bullet-}$ by CQD@Ag NCs

To further test the ability of fluorescent imaging of intracellular $O_2^{\bullet-}$, CQD@Ag NCs were incubated with MCF-7 cells. After incubating for 30 min, CQD@Ag NCs entered into cells and then EBSS without nutrient was incubated for another 30, 60, 90, and 120 min, respectively, inducing increasing production of $O_2^{\bullet-}$ [43]. The MCF-7 cells were observed by fluorescence microscopy with an excitation at 365 nm. As a control, whether or not induction of autophagy, CQDs always emitted blue fluorescence (Fig. 5a), suggesting CQDs are

fluorescence resistant in the $O_2^{\bullet-}$ circumstance and accumulation into cytoplasm of cells [44, 45]. There was no fluorescent signal of CQD@Ag NCs in normal cells indicating a low level of $O_2^{\bullet-}$, while blue fluorescence was observed during autophagy (Fig. 5a). The fluorescence from CQD@Ag NCs was first observed in MCF-7 cells after autophagy induction 30 min, and gradually increased with the progression of autophagy (Fig. 5a) suggesting gradually increasing $O_2^{\bullet-}$ concentration. The maximum fluorescence signal emerged at 90 min after autophagy induction (Fig. 5a).

To validate the relationship between fluorescence intensity and $O_2^{\bullet-}$ concentration, the relative fluorescence intensity, the ratio of CQD@Ag NC fluorescence intensity to CQDs (F/F_0) was counted (Fig. 5b). $O_2^{\bullet-}$ concentration was calculated according to the linear calibration equation: $F/F_0 = 0.55\ c(O_2^{\bullet-}) - 0.14$ (Fig. 5b), showing that the trend of fluorescence intensity was consistent with the $O_2^{\bullet-}$ concentration. Thus, fluorescent imaging of intracellular $O_2^{\bullet-}$ by CQD@Ag NCs could be used as an efficient detection method for monitoring the production of $O_2^{\bullet-}$ in living cells.

Fig. 5 a Fluorescence microscopy images of MCF-7 cells incubated with CQDs (100 μg mL^{-1}) and CQD@Ag NCs (100 μg mL^{-1}) for 30 min; after then, MCF-7 cells were induced with or without EBSS induction at different times (0, 30, 60, 90, 120 min). The scale bar is 100 μm. b The F/F_0 (the ratio of CQD@Ag NC fluorescence intensity to CQDs) and $O_2^{\bullet-}$ concentration at various induction times
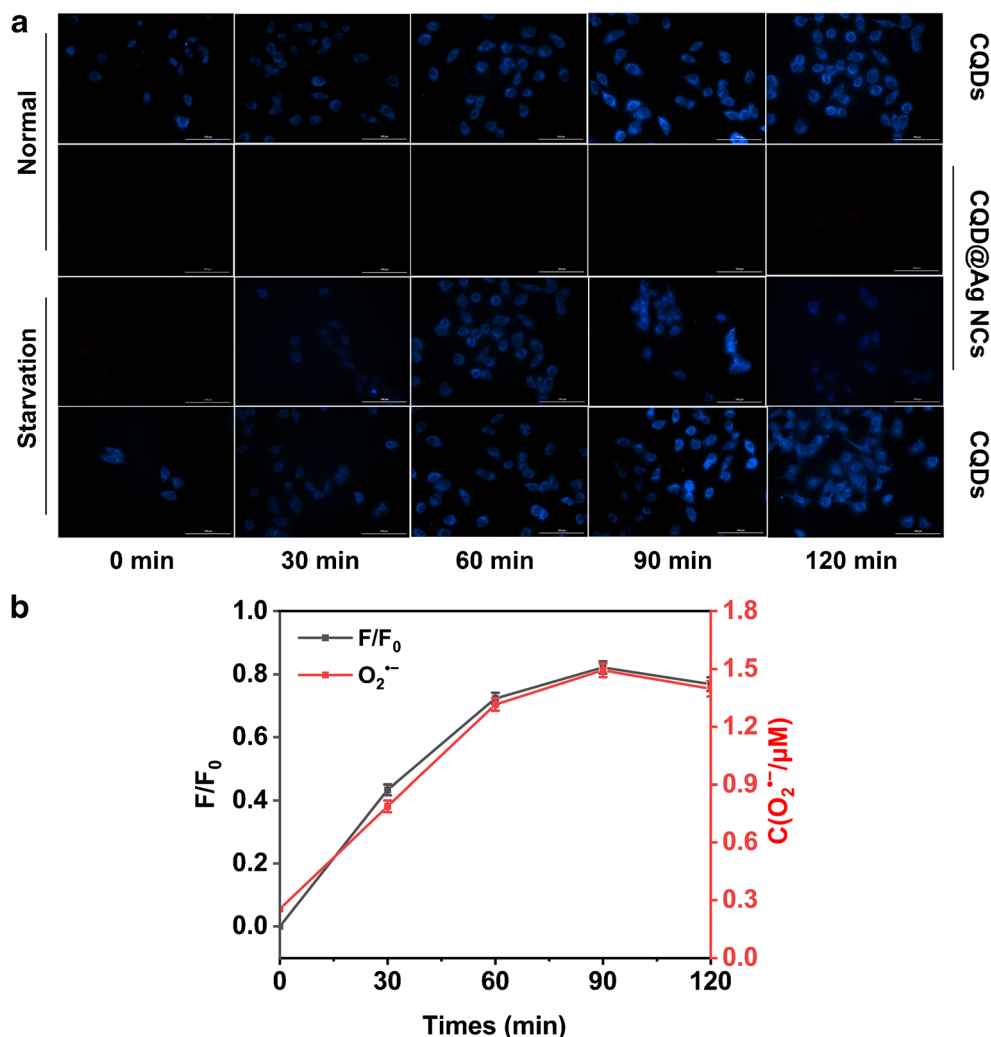
Compared with electrochemical detection (Table S1), a synthesized probe (CQD@Ag NCs) can directly detect the intracellular $O_2^{\bullet-}$ rather than extracellular $O_2^{\bullet-}$ released from the cells, which can improve the detection accuracy due to the rapid conversion of $O_2^{\bullet-}$. Like small molecule, ratiometric, and other fluorescent probes and near-infrared probes, the CQD@Ag NCs could be applied for fluorescence imaging of $O_2^{\bullet-}$. The excellent performance of the fluorescent assay is attributed to the use of the CQD@Ag NCs which avoids the complicated experimental procedure. The turn-on mode made the sensitive fluorescence imaging possible. However, the common problem in CQD@Ag NC fluorescent imaging is the background fluorescence. Near-infrared CQD fluorescence may offer a potential solution for the limitation [46].

Conclusion

A fluorescent "turn-on" assay for sensitive and selective imaging of intracellular $O_2^{\bullet-}$ was designed using CQD@Ag core-shell nanocomposites, which were easily synthesized by in situ reduction of Ag NPs onto CQDs. The fluorescence of CQDs was quenched by the Ag shell and recovered when the Ag shell was etched by $O_2^{\bullet-}$. The fluorescence response of CQD@Ag NCs to different concentrations of $O_2^{\bullet-}$ solution showed regular fluorescence recovery, exhibiting a good linear relationship ($R^2 = 0.993$) between the normalized fluorescence intensity and $O_2^{\bullet-}$ concentration, and a low detection limit (0.3 μM). This method was applied for fluorescent imaging of intracellular $O_2^{\bullet-}$ of cells during serum starvation–induced autophagy. Although fairly narrow in $O_2^{\bullet-}$ solution detection (0.6–1.6 μM), the linear range covers the detection range of $O_2^{\bullet-}$ in autophagy-induced cells. In view of the convenient synthesis, attractive fluorescence characteristics, and low cytotoxicity, the CQD@Ag NC–based strategy is a promising candidate for low cost, highly sensitive and selective cellular imaging, sensing, and labeling.

Compliance with ethical standards

Conflict of interest The authors declare that they have no competing interests.

References

1. Peng F, Xu T, Wu F, Ma C, Liu Y, Li J, Zhao B, Mao C (2017) Novel biomimetic enzyme for sensitive detection of superoxide anions. Talanta 174:82–91. https://doi.org/10.1016/j.talanta.2017.05.028

2. Gorrini C, Harris IS, Mak TW (2013) Modulation of oxidative stress as an anticancer strategy. Nat Rev Drug Discov 12(12):931–947. https://doi.org/10.1038/nrd4002

3. Labib M, Sargent EH, Kelley SO (2016) Electrochemical methods for the analysis of clinically relevant biomolecules. Chem Rev 116(16):9001–9090. https://doi.org/10.1021/acs.chemrev.6b00220

4. Liu X, Ran MM, Guoan XH, Xue ZH, Lu XQ (2018) A sensitively non-enzymatic amperometric sensor and its application in living cell superoxide anion radical detection. Talanta 186:248–255. https://doi.org/10.1016/j.talanta.2018.04.067

5. Li Y, Zhang H, Cai X, Zhao H, Magdassi S, Lan M (2019) Electrochemical detection of superoxide anions in HeLa cells by using two enzyme-free sensors prepared from ZIF-8-derived carbon nanomaterials. Microchim Acta 186(6):370. https://doi.org/10.1007/s00604-019-3473-y

6. Zheng J, Wang B, Jin Y, Weng B, Chen J (2019) Nanostructured MXene-based biomimetic enzymes for amperometric detection of superoxide anions from HepG2 cells. Microchim Acta 186(2):95. https://doi.org/10.1007/s00604-018-3220-9

7. Ying W, Lei MQ, Chen LL, Liu ZY, Bao YS (2018) FePO₄ embedded in nanofibers consisting of amorphous carbon and reduced graphene oxide as an enzyme mimetic for monitoring superoxide anions released by living cells. Microchim Acta 185(2):140. https://doi.org/10.1007/s00604-018-2691-z

8. Yang H, Hou J, Wang Z, Zhang T, Xu C (2018) An ultrasensitive biosensor for superoxide anion based on hollow porous PtAg nanospheres. Biosens Bioelectron 117:429–435. https://doi.org/10.1016/j.bios.2018.06.034

9. Zhang H, Cai X, Zhao H, Sun W, Wang Z, Lan M (2019) Enzyme-free electrochemical sensor based on ZIF-67 for the detection of superoxide anion radical released from SK-BR-3 cells. J Electroanal Chem 855:113653. https://doi.org/10.1016/j.jelechem.2019.113653

10. Liu Y, Liu X, Liu Y, Liu G, Ding L, Lu X (2017) Construction of a highly sensitive non-enzymatic sensor for superoxide anion radical detection from living cells. Biosens Bioelectron 90:39–45. https://doi.org/10.1016/j.bios.2016.11.015

11. Wildgoose GG, Banks CE, Compton RG (2006) Metal nanoparticles and related materials supported on carbon nanotubes: methods and applications. Small 2(2):182–193. https://doi.org/10.1002/smll.200500324

12. Liu Y, Wei H, Jiang X, Guo H, Liu X (2018) Synthesis of metal–organic frameworks derived nanocomposites for superoxide anion radical sensing and cell monitoring upon oxidative stress. J Electroanal Chem 820:51–59. https://doi.org/10.1016/j.jelechem.2018.04.068

13. Li N, Wang H, Xue M, Chang C, Chen Z, Zhuo L, Tang B (2012) A highly selective and sensitive nanoprobe for detection and imaging of the superoxide anion radical in living cells. Chem Commun 48(19):2507–2509. https://doi.org/10.1039/c2cc16376d

14. Robinson KM, Janes MS, Pehar M, Monette JS, Ross MF, Hagen TM, Murphy MP, Beckman JS (2006) Selective fluorescent imaging of superoxide in vivo using ethidium-based probes. PNAS 103(41):15038–15043. https://doi.org/10.1073/pnas.0601945103

15. Henderson LM, Chappell JB (1993) Dihydrorhodamine 123: a fluorescent probe for superoxide generation? Eur J Biochem 217(3):973–980. https://doi.org/10.1111/j.1432-1033.1993.tb18328.x

16. Gao X, Ding C, Zhu A, Tian Y (2014) Carbon-dot-based ratiometric fluorescent probe for imaging and biosensing of superoxide anion in live cells. Anal Chem 86(14):7071–7078. https://doi.org/10.1021/ac501499y

17. Zhou Y, Ding J, Liang T, Abdel-Halim ES, Jiang L, Zhu JJ (2016) FIT doped rattle-type silica colloidal particleatiometric fluorescent

sensor for biosensing and imaging of superoxide anion. ACS Appl Mater Interfaces 8:6423–6430. https://doi.org/10.1021/acsami.6b01031

18. Chen Z, Li J, Chen X, Cao J, Zhang J, Min Q, Zhu JJ (2015) Single gold@silver nanoprobes for real-time tracing the entire autophagy process at single-cell level. J Am Chem Soc 137(5):1903–1908. https://doi.org/10.1021/ja5112628

19. Lu D, Zhou L, Wang R, Zhang X-B, He L, Zhang J, Hu X, Tan W (2017) A two-photon fluorescent probe for endogenous superoxide anion radical detection and imaging in living cells and tissues. Sensors Actuators B Chem 250(2017):259–266. https://doi.org/10.1016/j.snb.2017.04.041

20. Yuan L, Lin W, Zheng K, Zhu S (2013) FRET-based small-molecule fluorescent probes: rational design and bioimaging applications. Acc Chem Res 46(7):1462–1473. https://doi.org/10.1021/ar300273v

21. Chen L, Cho MK, Wu D, Kim HM, Yoon J (2019) Two-photon fluorescence probe for selective monitoring of superoxide in live cells and tissues. Anal Chem 91(22):14691–14696. https://doi.org/10.1021/acs.analchem.9b03937

22. Xi Z, Yuan F, Wang Z, Li S, Fan L (2018) Highly efficient and stable full-color random lasing emission based on carbon quantum dots. Acta Chim Sin 76(6):460. https://doi.org/10.6023/A18020048

23. Singh V, Rawat K, Mishra S, Baghel T, Fatima S (2018) Biocompatible fluorescent carbon quantum dots prepared from beetroot extract for in vivo live imaging in C-elegans and BALB/c mice. J Mater Chem B 6(20):3366–3371. https://doi.org/10.1039/c8tb00503f

24. Wang WJ, Xia JM, Feng J, He MQ, Chen ML, Wang JH (2016) Green preparation of carbon dots for intracellular pH sensing and multicolor live cell imaging. J Mater Chem B 4(44):7130–7137. https://doi.org/10.1039/c6tb02071b

25. Sharma V, Kaur N, Tiwari P, Mobin SM (2018) Full color emitting fluorescent carbon material as reversible pH sensor with multicolor live cell imaging. J Photochem Photobiol B 182:137–145. https://doi.org/10.1016/j.jphotobiol.2018.04.006

26. Ma JL, Yin BC, Wu X, Ye BC (2017) Simple and cost-effective glucose detection based on carbon nanodots supported on silver nanoparticles. Anal Chem 89(2):1323–1328. https://doi.org/10.1021/acs.analchem.6b04259

27. Gul U, Kanwal S, Tabassum S, Gilani MA, Rahim A (2020) Microwave-assisted synthesis of carbon dots as reductant and stabilizer for silver nanoparticles with enhanced-peroxidase like activity for colorimetric determination of hydrogen peroxide and glucose. Microchim Acta 187(2):135. https://doi.org/10.1007/s00604-019-4098-x

28. Wu S, Kong XJ, Cen Y, Yuan J, Yu RQ, Chu X (2016) Fabrication of a LRET-based upconverting hybrid nanocomposite for turn-on sensing of H₂O₂ and glucose. Nanoscale 8(16):8939–8946. https://doi.org/10.1039/c6nr00470a

29. Walekar LS, Hu P, Liao F, Guo X, Long M (2017) Turn-on fluorometric and colorimetric probe for hydrogen peroxide based on the in-situ formation of silver ions from a composite made from N-doped carbon quantum dots and silver nanoparticles. Microchim Acta 185(1):31. https://doi.org/10.1007/s00604-017-2545-0

30. Kong RM, Yang A, Wang Q, Wang Y, Ma L, Qu F (2018) Uricase based fluorometric determination of uric acid based on the use of graphene quantum dot@silver core-shell nanocomposites. Microchim Acta 185(63). https://doi.org/10.1007/s00604-017-2614-4

31. Kasprzyk W, Swiergosz T, Bednarz S, Walas K, Bashmakova NV, Bogdal D (2018) Luminescence phenomena of carbon dots derived from citric acid and urea - a molecular insight. Nanoscale 10(29):13889–13894. https://doi.org/10.1039/c8nr03602k

32. Ge B, Lisdat F (2002) Superoxide sensor based on cytochrome c immobilized on mixed-thiol SAM with a new calibration method. Anal Chim Acta 454(1):53–64. https://doi.org/10.1016/S0003-2670(01)01545-8

33. Maeda H, Yamamoto K, Nomura Y, Kohno I, Hafsi L, Ueda N, Yoshida S, Fukuda M, Fukuyasu Y, Yamauchi Y, Itoh N (2005) A design of fluorescent probes for superoxide based on a nonredox mechanism. J Am Chem Soc 127(1):68–69. https://doi.org/10.1021/ja047018k

34. Hu JJ, Wong NK, Ye S, Chen X, Lu MY, Zhao AQ, Guo Y, Ma AC, Leung AY, Shen J, Yang D (2015) Fluorescent probe HKSOX-1 for imaging and detection of endogenous superoxide in live cells and in vivo. J Am Chem Soc 137(21):6837–6843. https://doi.org/10.1021/jacs.5b01881

35. Li J, Zhang B, Wang F, C-y L (2011) Silver/carbon-quantum-dot plasmonic luminescent nanoparticles. New J Chem 35(3):554. https://doi.org/10.1039/c0nj01027h

36. Xia J, Di J, Li H, Xu H, Li H, Guo S (2016) Ionic liquid-induced strategy for carbon quantum dots/BiOX (X=Br, Cl) hybrid nanosheets with superior visible light-driven photocatalysis. Appl Catal B 181:260–269. https://doi.org/10.1016/j.apcatb.2015.07.035

37. Liu L, Gao Z, Jiang B, Bai Y, Wang W, Yin Y (2018) Reversible assembly and dynamic plasmonic tuning of Ag nanoparticles enabled by limited ligand protection. Nano Lett 18(8):5312–5318. https://doi.org/10.1021/acs.nanolett.8b02325

38. Zhan Y, Geng T, Liu Y, Hu C, Zhang X, Lei B, Zhuang J, Wu X, Huang D, Xiao G, Zou B (2018) Near-ultraviolet to near-infrared fluorescent nitrogen-doped carbon dots with two-photon and piezochromic luminescence. ACS Appl Mater Interfaces 10(33):27920–27927. https://doi.org/10.1021/acsami.8b07498

39. Han J, Liu Z, Guo Y, Han G-C, Li W, Chen S, Zhang S (2017) Determination of superoxide anion radical by modified CdTe quantum dots. J Photochem Photobiol A 349:1–6. https://doi.org/10.1016/j.jphotochem.2017.08.049

40. Li Z, Xiao L (2017) Facile sonochemical synthesis of water-soluble gold nanodots as fluorescent probes for superoxide radical anion detection and cell imaging. Anal Methods 9(12):1920–1927. https://doi.org/10.1039/c6ay03294j

41. Li P, Liu L, Xiao H, Zhang W, Wang L, Tang B (2016) A new polymer nanoprobe based on chemiluminescence resonance energy transfer for ultrasensitive imaging of intrinsic superoxide anion in mice. J Am Chem Soc 138(9):2893–2896. https://doi.org/10.1021/jacs.5b11784

42. Song Y, Hao J, Hu D, Zeng M, Li P, Li H, Chen L, Tan H, Wang L (2017) Ratiometric fluorescent detection of superoxide anion with polystyrene@nanoscale coordination polymers. Sensors Actuators B Chem 238:938–944. https://doi.org/10.1016/j.snb.2016.04.181

43. Li L, Chen Y, Gibson SB (2013) Starvation-induced autophagy is regulated by mitochondrial reactive oxygen species leading to AMPK activation. Cell Signal 25(1):50–65. https://doi.org/10.1016/j.cellsig.2012.09.020

44. Sachdev A, Matai I, Gopinath P (2015) Dual-functional carbon dots-silver@zinc oxide nanocomposite: in vitro evaluation of cellular uptake and induction of apoptosis. J Mater Chem B 3(7):1217–1229. https://doi.org/10.1039/c4tb02043j

45. Tang M, Teng P, Long Y, Wang X, Liang L, Shen D, Wang J, Zheng H (2018) Hollow carbon dots labeled with FITC or TRITC for use in fluorescent cellular imaging. Microchim Acta 185(4):223. https://doi.org/10.1007/s00604-018-2761-2

46. Shi X, Meng H, Sun Y, Qu L, Lin Y, Li Z, Du D (2019) Far-red to near-infrared carbon dots: preparation and applications in biotechnology. Small 15(48):1901507. https://doi.org/10.1002/smll.201901507